

ARTICLE

<https://doi.org/10.1038/s42005-019-0247-0>

OPEN

Possible strain induced Mott gap collapse in $1T\text{-TaS}_2$

Kunliang Bu¹, Wenhao Zhang¹, Ying Fei¹, Zongxiu Wu¹, Yuan Zheng¹, Jingjing Gao^{2,3}, Xuan Luo², Yu-Ping Sun^{2,4,5} & Yi Yin^{1,5*}

Tuning the electronic properties of a matter is of fundamental interest in scientific research as well as in applications. Recently, the Mott insulator-metal transition has been reported in a pristine layered transition metal dichalcogenide $1T\text{-TaS}_2$, with the transition triggered by an optical excitation, a gate controlled intercalation, or a voltage pulse. However, the sudden insulator-metal transition hinders an exploration of how the transition evolves. Here, we report the strain as a possible new tuning parameter to induce Mott gap collapse in $1T\text{-TaS}_2$. In a strain-rich area, we find a mosaic state with distinct electronic density of states within different domains. In a corrugated surface, we further observe and analyze a smooth evolution from a Mott gap state to a metallic state. Our results shed new lights on the understanding of the insulator-metal transition and promote a controllable strain engineering on the design of switching devices in the future.

¹Zhejiang Province Key Laboratory of Quantum Technology and Device, Department of Physics, Zhejiang University, 310027 Hangzhou, China. ²Key Laboratory of Materials Physics, Institute of Solid State Physics, Chinese Academy of Sciences, 230031 Hefei, China. ³University of Science and Technology of China, 230026 Hefei, China. ⁴High Magnetic Field Laboratory, Chinese Academy of Sciences, 230031 Hefei, China. ⁵Collaborative Innovation Center of Advanced Microstructures, Nanjing University, 210093 Nanjing, China. *email: yiyin@zju.edu.cn

For a half-filled electronic band, strong correlation of electrons can lead to a unique Mott insulator state, when the ratio of Coulomb repulsion U to the bandwidth W (U/W) exceeds a critical value¹. Proximity to the Mott insulator is the origin of many exotic superconducting states, such as in cuprates², magic-angle graphenes^{3,4} and transition metal dichalcogenides^{5–7}. To explore the superconducting mechanism, it is important to understand the Mott insulator state and how the transition evolves from a Mott insulator to a metallic or superconducting state⁸.

The transition metal dichalcogenide $1T\text{-TaS}_2$ is a correlation-induced Mott insulator^{5–7}. The Mott insulator state of $1T\text{-TaS}_2$ is not residing in a periodic atomic lattice, but in a periodic commensurate charge density wave (CCDW) lattice. With the CDW state susceptible to external perturbations, the Mott insulator state is relatively easy to be modulated^{9,10}. The Mott phase of the pristine $1T\text{-TaS}_2$ can be suppressed by chemical doping^{11–15}, intercalation^{16,17}, thermal excitation¹⁸, or pressure⁵. Recently, the Mott insulator-metal transition has been further controlled by an optical excitation^{19,20}, gate controlled intercalation⁹, or a charge pulse^{20–25}. Although the underlying mechanism of insulator-metal transition is still under debate, these controlled tuning methods are good candidates for the design of switching devices. Insightful information has been reported to tune the electronic states of complex materials by strain^{26–35}.

In this study, we show a possible strain-induced Mott-gap collapse in the pristine $1T\text{-TaS}_2$ by scanning tunneling microscopy (STM). In a strain-rich area, we find mosaic CDW domains and the stable mosaic state is most possibly induced by the intrinsic strain. In the mosaic state, we could detect variable spectra from a Mott gap state to a metallic state within different domains. We further find a corrugated surface, also possibly a strain-induced feature. When being across the corrugation, a smooth evolution of the Mott-gap collapse is observed and analyzed. The Mott gap is suppressed gradually and a V-shaped metallic state emerges at the corrugation. In the process of Mott-gap collapse, the rapid increase of bandwidth W is found to be the dominant factor to reduce U/W . By gluing $1T\text{-TaS}_2$ on the organic-glass substrate, we introduce strain to the sample surface at low temperature, and confirm the strain-induced mosaic pattern and corrugation. Our results provide a further understanding of the Mott insulator-metal transition and suggest the strain engineering as a possible new tuning method to modulate the Mott insulator state.

Results

Crystal structure and electronic state of the pristine $1T\text{-TaS}_2$. The unit structure of $1T\text{-TaS}_2$ is composed of a triangular lattice of Ta atoms sandwiched between two layers of triangular lattice of S atoms. With an ABC-type stacking, each Ta atom is coordinated octahedrally by S atoms. The sample is at near commensurate CDW (NCCDW) state at room temperature and develops to the CCDW state at around 170 K (Supplementary Fig. 1). A basic element of the CDW state is the so called Star of David (SOD). As shown in Fig. 1a, the SOD cluster is formed by 13 Ta atoms with 12 surrounding Ta atoms shrinking to the central Ta. At the CCDW state, the SODs are regularly arranged to form a $\sqrt{13} \times \sqrt{13}$ reconstruction^{36–38}. With the single crystal sample cleaved and a top S layer exposed, the STM experiment is performed on the exposed surface at liquid helium temperature around 4.5 K.

A typical topography is shown in Fig. 1b, with each bright spot representing a SOD. Consistent with the $\sqrt{13} \times \sqrt{13}$ reconstruction, the bright spots form a triangular lattice of SODs and the distance of two neighboring SODs is measured to be 12.1 Å. A

single unpaired $5d$ electron of the central Ta atom in each SOD contributes to the half-filled electronic band, leading to the Mott insulator state of the pristine $1T\text{-TaS}_2$. In the field of view (FOV) in Fig. 1b, a differential conductance (dI/dV) spectrum is measured at each point in a dense grid of spatial positions. The average spectrum is shown in Fig. 1c. With the spectrum proportional to the electronic density of states (DOS), the sharp coherence peaks at 240 mV and -200 mV correspond to the upper and lower Hubbard bands (UHB and LHB), respectively¹¹. Energy positions of UHB and LHB result in a Mott gap of 440 ± 20 meV. In the average spectrum, there is also a broad peak at -460 mV and a kink feature at 440 mV, corresponding to the valence band (VB) peak and the conduction band (CB) peak of the CDW gap, respectively^{11,39}. All these characteristics are consistent with previous reports of the pristine $1T\text{-TaS}_2$ ^{15,24,25,39,40}.

Stable mosaic state in a strain-rich area. We intentionally look for a strain-rich area. Fig. 1d is a topographic image of a $100 \text{ nm} \times 100 \text{ nm}$ area. The complex morphology indicates a strain-rich environment around this area, which may originate from the cleavage process. A zoom-in image of the white box shows a mosaic state with several nanometer-sized domains (Fig. 1e). The textured domains are different from the quasi-hexagonal phase in the NCCDW state^{41,42}. The pattern shows that they are more similar to the voltage pulse induced mosaic state^{24,25}. Within each domain, the superlattice of SODs is still preserved. Neighboring domains are separated by bright domain walls, across which there is a translational phase shift of the CDW order. We do not see any rotational shift of the CDW order between different domains¹⁵. This mosaic state is stable at 4.5 K, without any change after a longtime measurement. With the temperature increased to 60 K (Fig. 1f), the domain wall pattern is almost the same as that at low temperature (see more details in Supplementary Figs. 2 and 3). Different from the metastable mosaic state triggered by a voltage pulse^{24,25}, this mosaic state in strain-rich area is very stable, possibly attributed to the intrinsic and stable strain.

Electronic states in mosaic domains. Figure 2a, b show conductance maps of the mosaic domains under a bias voltage of -200 mV and 0 mV, respectively. The bias voltage of -200 mV is chosen to be at the peak position of LHB. The pattern of mosaic domains can be clearly observed in Fig. 2a, with the domain walls one-to-one mapped to Fig. 2b (white dashed lines). Five typical dI/dV spectra are taken within different domains, at labeled positions (Fig. 2c). For the position marked by '1', the dI/dV spectrum shows a Mott insulator state, with sharp coherence peaks of LHB and UHB. For spectra at positions marked from '2' to '5', the differential conductance at -200 mV decreases, the Mott gap is suppressed to a V-shaped gap, and the V-shaped gap develops together with a finite DOS at zero bias (Fermi energy E_F). A V-shaped gap has been observed in Cu intercalated $1T\text{-TaS}_2$, and the gap gradually disappears with the increase of temperature¹⁷. A similar V-shaped gap has also been observed in isovalent Se doped $1T\text{-TaS}_2$ ¹⁵.

The variation of dI/dV spectra is consistent with the conductance map in Fig. 2a, in which the domain marked by '1' is represented by a bright white patch and different from other purple patches. We notice that the conductance is relatively uniform within each domain in Fig. 2a, and the periodic pattern in the domain is still consistent with the CCDW superlattice. For conductance at E_F , both a zero conductance and a finite conductance are observed in the dI/dV spectra in Fig. 2c, with the latter representing a metallic state (olive and blue curves). Within each single domain, the zero bias conductance at the clean

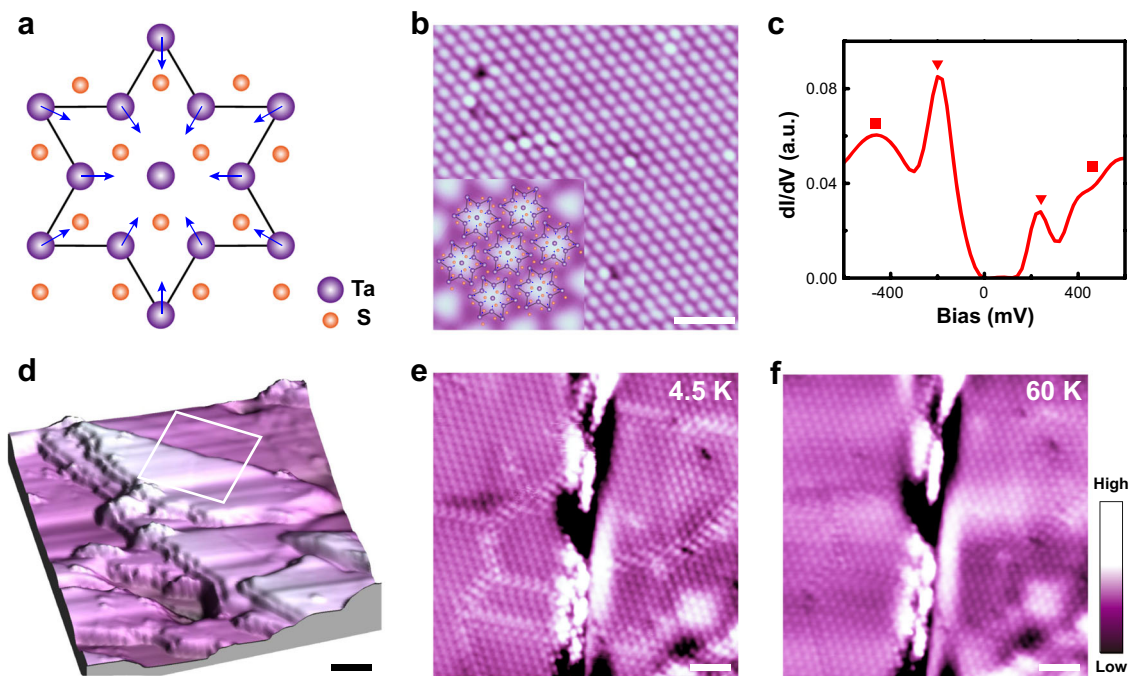


Fig. 1 Stable mosaic state in 1T-TaS₂. **a** Schematic structure of a Star of David (SOD). The purple and yellow balls represent the Ta and S atoms, respectively. The blue arrows indicate that the 12 surrounding Ta atoms shrink to the central Ta atom. **b** A typical topography of 25 nm × 25 nm in a clean area. Inset shows a 4 nm × 4 nm image with the schematic structure of SODs superimposed on it. The tunneling condition is $V_b = 600$ mV and $I = 100$ pA. **c** Average dI/dV spectra simultaneously taken with **b**. The bias modulation is set to be 10 mV. The inverted triangles and squares indicate coherence peaks of Mott gap and charge density wave (CDW) gap, respectively. **d** A three dimensional plot of the topography over a 100 nm × 100 nm area. The tunneling condition is $V_b = 1$ V and $I = 20$ pA. **e, f** The enlargement of the white box (38 nm × 38 nm) at 4.5 K (**e**) and at 60 K (**f**). The tunneling condition is $V_b = 600$ mV, $I = 300$ pA in **e**, and $V_b = 1$ V, $I = 200$ pA in **f**. Scale bar is 10 nm in **d** and 5 nm in **b, e, and f**

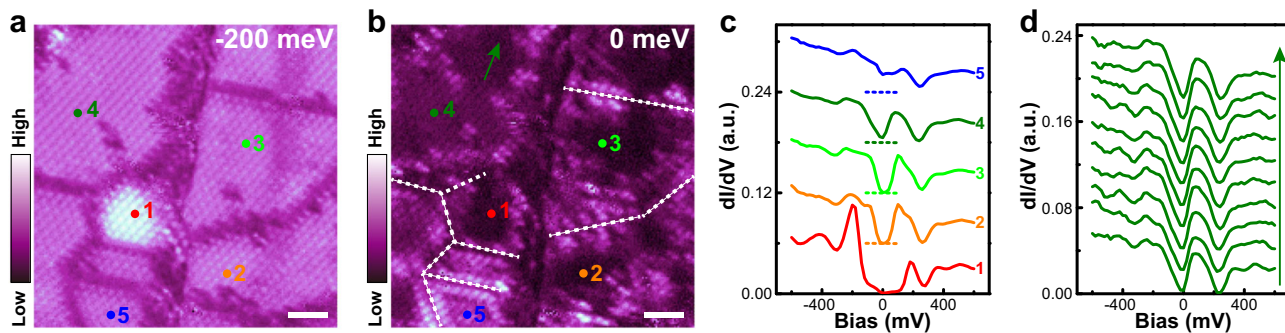


Fig. 2 Electronic states of mosaic domains. **a, b** The differential conductance maps at -200 meV (the energy of lower Hubbard band) and 0 meV (Fermi energy), respectively. Scale bar is 5 nm. The field of view is approximately the same as that in Fig. 1e and f. The white dashed lines in **b** illustrate the domain walls. **c** The dI/dV spectra at marked positions in **a** and **b**. The dataset is shifted vertically for clarity. The short dashed lines represent the zero vertical coordinate of shifted curves. **d** A series of dI/dV spectra taken along the olive arrow in **b**. All spectra are taken at $V_b = 600$ mV and $I = 100$ pA, with a bias modulation of 10 mV

area is also homogeneous, as shown in Fig. 2d. Some of the bright features in Fig. 2b are due to the CDW impurities like missing or distorted SOD. Other bright patches in Fig. 2b aggregate at the step edge and the edge of each domain. There may be a mechanism that leads to trapped carriers at the edges of domains, which is however not clear yet.

Mott-gap collapse at a corrugation. The mosaic domains and related complex electronic states are speculated to be induced by the intrinsic strain. We further find an area with a corrugated surface, not far away from the strain-rich area (Supplementary Fig. 4). The corrugation is also a possible strain-induced feature^{43,44}. In this corrugated area, we observe a smooth

evolution of Mott-gap collapse across the corrugation, which gives us a special example to analyze the Mott insulator-metal transition.

Figure 3a shows a topographic image of the corrugated surface, from which we could observe a periodic and triangular lattice of SODs without any domain wall. This FOV is within a single domain. Bright and dark stripes appear roughly along the diagonal direction, representing a corrugated surface with a modulation of z -axis height. We focus on a straight line across central stripes (the white arrowed line in Fig. 3a). In Fig. 3b, the surface height is drawn as a function of distance along the line, in which the ups and downs correspond to the bright and dark stripes in the two-dimensional topograph. A flat surface is shaped into a corrugation with parallel ridges and grooves. The height of

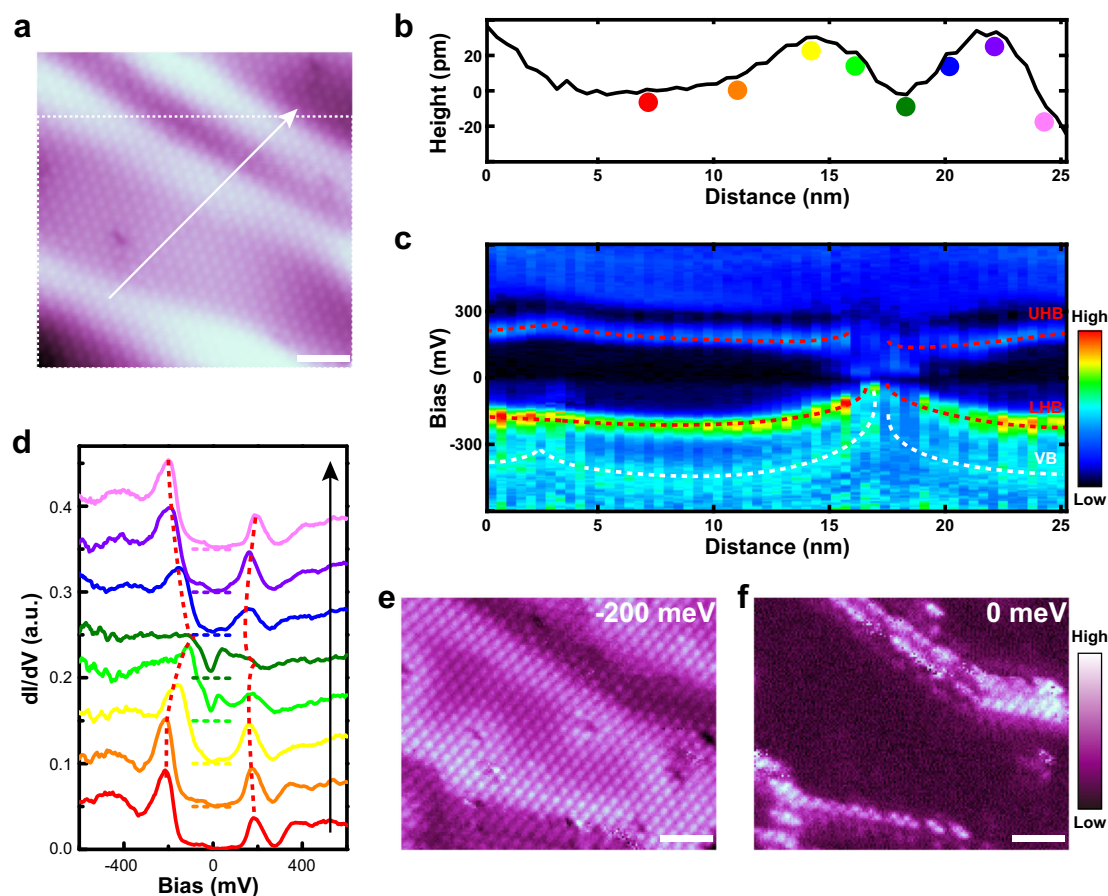


Fig. 3 Mott-gap collapse across the corrugation. **a** A topographic image with corrugations (30 nm \times 30 nm). The tunneling condition is $V_b = 1$ V and $I = 200$ pA. **b** The height profile along the white arrowed line in **a**. The height profile is obtained from collected tip height value in the topography, with a linear background subtraction. **c** The acquired dI/dV spectra along the height profile, as a function of the distance along the arrowed line. The red and white dashed lines guide eyes to the Hubbard bands and valence band, respectively. The spectra are taken with a tunneling condition of $V_b = 600$ mV, $I = 100$ pA and a bias modulation of 10 mV. **d** The dI/dV spectra corresponding to the positions marked by colored dots in **b**. The red dashed lines guide eyes to the evolution of Hubbard bands. **e, f** Differential conductance maps at -200 meV and the Fermi level, respectively. The field of view is the same as the white dashed box in **a**. The conductance map is taken at $V_b = 600$ mV and $I = 100$ pA, with a bias modulation of 10 mV. Scale bar in **a, e**, and **f** is 5 nm

the corrugation is in the range of tens of picometers, comparably small as that of other stain-induced corrugations^{44–46}. Without an atomic resolution in this experiment, we cannot make a quantitative analysis of the strain based on precise determination of atomic displacement^{34,46}.

We measure a series of dI/dV spectra along the straight line, with data shown in Fig. 3c. Some typical spectra are selectively chosen and shown in Fig. 3d. The location of each spectrum is labeled by a colored dot in the height profile (Fig. 3b). Approaching the dark groove from both sides, we could observe a smooth evolution of Mott-gap collapse. Both UHB and LHB peaks move gradually toward the zero bias (Fermi energy E_F), with peak height decreases and peak width increases. The energy range of zero conductance shrinks until an in-gap state develops to form a metallic V-shaped spectrum. From the smooth evolution of spectra, we can track how the Hubbard band peaks evolve when approaching the groove. In the metallic state, the Hubbard band peaks are separated from two V-spectrum peaks. In Fig. 3c, another important feature is that the VB peak moves toward the zero bias together with the LHB peak, and finally merges to form the V-shaped spectrum.

To check the detailed distribution of the Mott-gap collapse in this corrugated area, we choose a framed area in Fig. 3a and measure the dI/dV spectra at a dense array of locations. Figure 3e, f show conductance maps at -200 mV and 0 mV,

respectively. Consistent with previous linecut spectra, metallic state in the shallow groove corresponds to a dark depression in Fig. 3e and a bright protrusion in Fig. 3f. In contrast, the Mott insulator state outside the groove shows a strong LHB peak (bright color in Fig. 3e) and a zero conductance around the Fermi energy (dark color in Fig. 3f). An additional metallic state at the left bottom corner in Fig. 3f may be due to the complex trough there, as indicated by the large depression at the same position in Fig. 3a.

Discussion

A Mott insulator-metal transition can be generally explained by a reduced ratio of U/W in the one-band Hubbard model. The change of U can be represented by a change of the Mott gap. For the linecut spectra in Fig. 3c, we fit both UHB and LHB peaks of each spectrum with a Gaussian function (Supplementary Fig. 5) and extract their energy positions and bandwidths. As shown in Fig. 4, the bandwidth of LHB is consistently larger than that of UHB, indicating a higher hopping constant t for LHB (t is proportional to W). When approaching the groove from the left side, we could observe that the Mott gap gradually decreases while the bandwidth of both UHB and LHB peaks is nearly unchanged (brown region). Here, the decrease of U is mainly responsible for the reduced U/W . When being closer to the groove (purple

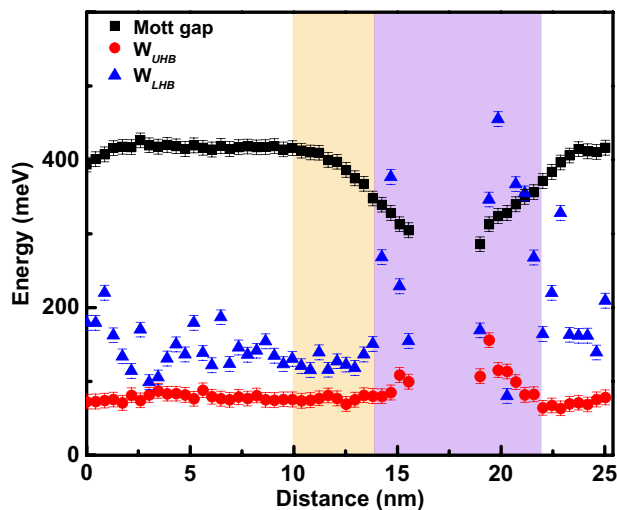


Fig. 4 Evolution of the electronic states across the corrugation. The dI/dV spectra in Fig. 3c are fitted by a Gaussian function, to extract the Mott gap, bandwidth of upper Hubbard band (UHB) and bandwidth of lower Hubbard band (LHB) (represented by black squares, red dots and blue triangles, respectively). The data in the vicinity of the groove cannot be fitted reasonably, correspondingly not shown. The error bars for the measured data points are due to the bias modulation. Within the brown region, the Mott gap is gradually reduced and the bandwidth is nearly unchanged. For the purple region, the Mott gap is reduced together with a rapid increase of the bandwidth of LHB

region), the VB gradually merges with LHB and the LHB bandwidth rapidly increases. The increase of UHB bandwidth is accompanied by the development of in-gap state and the V-shaped spectrum. Although U still decreases in this region, the increase of bandwidth is observed to be the dominant factor to reduce U/W .

In ref. ¹⁵, a multi-orbital Hubbard model has been proposed, including contributions both from the central Ta orbital and the edge orbital of surrounding Ta atoms. With the one-band Hubbard model as a down-folded version of the multi-orbital model, the reduction of U/W is explained to be both from the decrease of U (of central Ta orbital) and from the decrease of on-site energy difference between two orbitals. The change of U can be represented by a change of the Mott gap, and the on-site energy difference between two orbitals can be represented by the relative position between VB and LHB peaks. Consistent with this two-orbital model, our observation reveals that the rapid increase of W happens together with the merge between VB and LHB, which is the main factor to reduce U/W and induce a metallic state. The smooth spectrum evolution in our corrugated surface provides a clear picture of how the Mott insulator-metal transition gradually happens. A Mott-gap collapse could also happen on the intrinsic domain walls^{40,47,48}, which is however a sharp transition that we cannot obtain a similar analysis as in Fig. 4 (see Supplementary Note 1). The single domain in the topographic image of the corrugated surface also proves that this Mott-gap collapse is a new phenomenon different from that induced by the domain-wall.

We also find another corrugation at this sample, which shows similar Mott-gap collapse at the corrugation (Supplementary Fig. 6). The merge of the VB and LHB is reproduced at this corrugation. We further conducted experiment on the ‘strained sample’ by gluing 1T-TaS₂ on the organic glass substrate. With a large thermal expansion coefficient of the substrate, a compressive strain is expected to act on the sample at low temperatures. The mosaic state and the corrugation are both confirmed in the

‘strained sample’ (Supplementary Figs. 7 and 8). We also conducted the experiment on samples glued on the SiO₂ (0001) substrate, which has a rather small thermal expansion coefficient and is expected to bring a tensile strain to the glued sample. Instead of corrugations, cracks are the dominant features on the surface for samples glued on the SiO₂ (0001) substrate. The precise position of the Mott-gap collapse cannot be simply concluded from the height profile of corrugations. The atomic-resolved topography is required for the microscopic analysis of the strain distribution in a corrugation, which is however technically challenging. Therefore to answer how or whether the strain as an underlying mechanism tunes the Mott-gap collapse is still beyond our current capabilities. Nevertheless, the observation of the similar behavior in the ‘strained sample’ suggests that the stable mosaic state and the corrugation can be generated as a response to the strain.

The mosaic state is a very complex phenomenon. Following we discuss possible roles of strain for the mosaic state. For the mosaic state, an energy cost is required to create domain walls. Strain may help to overcome the energy barrier for the creation of domain walls. Then the mosaic state can be initially generated as a response to the strain. Other techniques like laser pulse or tip-current pulse can similarly help to create domain walls and mosaic state in this material. No matter how the mosaic pattern is created, the metallic state in mosaic pattern can be similarly related with the destruction of the long range CCDW order. Afterwards, a global strain may possibly make the domain pattern energetically stable. A strain can tune the electronic states while preserves the overall flat atomic plane³⁴, like the rather weak spatial height modulation within the mosaic state. Another proposal to explain the mosaic state is that the stacking order tunes the Mott insulator-metal transition^{24,25}. The stacking order is variable according to the SOD misalignment along the crystalline c axis^{49,50}. In this experiment, we did not observe any domain wall underneath the top layer, thus cannot provide evidence for the stacking order proposal. A single uniform domain of Mott insulator state exists in the strain-rich area (Fig. 2), which may be related with the stacking order effect.

In conclusion, we have carefully studied the strain-induced corrugation and mosaic state in 1T-TaS₂. The smooth evolution of spectrum in corrugated surface provides a clear picture of how the Mott gap collapses. The mosaic state and the corrugation is further confirmed in the ‘strained sample’. A controllable strain engineering should be explored in the future to tune the electronic phases of 1T-TaS₂.

Methods

Sample preparation. The high quality 1T-TaS₂ single crystals were grown by the chemical vapor transport (CVT) method with iodine as the transport agent. Ta (99.99%, Aladdin) and S (99.99%, Aladdin) powders with mole ratio of 1:2 were weighted and mixed with 0.2 g of I₂, which were placed into silicon quartz tubes. These tubes were sealed under high vacuum and heated for 10 days in a two-zone furnace, where the temperature of source and growth zones were fixed at 850 °C and 750 °C, respectively. Then the quartz tubes were removed from the furnace and quenched in ice water mixture.

STM measurement. The STM and STS experiments were carried out in a commercial STM system⁵¹. The samples were gradually cooled to liquid nitrogen temperature and in situ cleaved. An electrochemically etched tungsten tip was treated with e-beam sputtering and field emission on a single crystalline with an Au (111) surface. A constant current scanning mode maintained by a feedback loop control was used in this experiment. The dI/dV spectra were taken with a standard lock-in technique with a frequency of 983.4 Hz and an amplitude of 10 mV. The dI/dV spectra at domain walls were taken with a bias modulation of 2 mV. All data were acquired at liquid helium temperature (~4.5 K) except for special statement.

Data availability

The source data and related supporting information are available upon reasonable request from the corresponding author.

Received: 1 April 2019; Accepted: 28 October 2019;

Published online: 21 November 2019

References

- Mott, N. F. Metal-insulator transition. *Rev. Mod. Phys.* **40**, 677–683 (1968).
- Lee, P. A., Nagaosa, N. & Wen, X. G. Doping a Mott insulator: physics of high-temperature superconductivity. *Rev. Mod. Phys.* **78**, 17–85 (2006).
- Cao, Y. et al. Unconventional superconductivity in magic-angle graphene superlattices. *Nature* **556**, 43–50 (2018).
- Cao, Y. et al. Correlated insulator behaviour at half-filling in magic-angle graphene superlattices. *Nature* **556**, 80–84 (2018).
- Sipos, B. et al. From Mott state to superconductivity in 1T-TaS₂. *Nat. Mater.* **7**, 960–965 (2008).
- Li, L. J. et al. Fe-doping-induced superconductivity in the charge-density-wave system 1T-TaS₂. *Europhys. Lett.* **97**, 67005 (2012).
- Liu, Y. et al. Superconductivity induced by Se-doping in layered charge-density-wave system 1T-TaS_{2-x}Se_x. *Appl. Phys. Lett.* **102**, 192602 (2013).
- Cai, P. et al. Visualizing the evolution from the Mott insulator to a charge-ordered insulator in lightly doped cuprates. *Nat. Phys.* **12**, 1047–1051 (2016).
- Yu, Y. J. et al. Gate-tunable phase transitions in thin flakes of 1T-TaS₂. *Nat. Nanotechnol.* **10**, 270–276 (2015).
- Tsen, A. W. et al. Structure and control of charge density waves in two-dimensional 1T-TaS₂. *Proc. Natl Acad. Sci. USA* **112**, 15054–15059 (2015).
- Ang, R. et al. Real-space coexistence of the melted Mott state and superconductivity in Fe-substituted 1T-TaS₂. *Phys. Rev. Lett.* **109**, 176403 (2012).
- Ang, R. et al. Superconductivity and bandwidth-controlled Mott metal-insulator transition in 1T-TaS_{2-x}Se_x. *Phys. Rev. B* **88**, 115145 (2013).
- Ang, R. et al. Atomistic origin of an ordered superstructure induced superconductivity in layered chalcogenides. *Nat. Commun.* **6**, 6091 (2015).
- Fujisawa, Y. et al. Appearance of a domain structure and its electronic states in iron doped 1T-TaS₂ observed using scanning tunneling microscopy and spectroscopy. *J. Phys. Soc. Jpn.* **86**, 113703 (2017).
- Qiao, S. et al. Mottness collapse in 1T-TaS_{2-x}Se_x transition-metal dichalcogenide: an interplay between localized and itinerant orbitals. *Phys. Rev. X* **7**, 041054 (2017).
- Wagner, K. E. et al. Tuning the charge density wave and superconductivity in Cu_xTaS₂. *Phys. Rev. B* **78**, 104520 (2008).
- Lahoud, E., Meetei, O. N., Chaska, K. B., Kanigel, A. & Trivedi, N. Emergence of a novel pseudogap metallic state in a disordered 2D Mott insulator. *Phys. Rev. Lett.* **112**, 206402 (2014).
- Di Salvo, F. J., Wilson, J. A., Bagley, B. G. & Waszczak, J. V. Effects of doping on charge-density waves in layer compounds. *Phys. Rev. B* **12**, 2220–2235 (1975).
- Stojchevska, L. et al. Ultrafast switching to a stable hidden quantum state in an electronic crystal. *Science* **344**, 177–180 (2014).
- Vaskivskiy, I. et al. Controlling the metal-to-insulator relaxation of the metastable hidden quantum state in 1T-TaS₂. *Sci. Adv.* **1**, e1500168 (2015).
- Hollander, M. J. et al. Electrically driven reversible insulator-metal phase transition in 1T-TaS₂. *Nano Lett.* **15**, 1861–1866 (2015).
- Yoshida, M., Suzuki, R., Zhang, Y. J., Nakano, M. & Iwasa, Y. Memristive phase switching in two-dimensional 1T-TaS₂ crystals. *Sci. Adv.* **1**, e1500606 (2015).
- Vaskivskiy, I. et al. Fast electronic resistance switching involving hidden charge density wave states. *Nat. Commun.* **7**, 11442 (2016).
- Cho, D. et al. Nanoscale manipulation of the Mott insulating state coupled to charge order in 1T-TaS₂. *Nat. Commun.* **7**, 10453 (2016).
- Ma, L. G. et al. A metallic mosaic phase and the origin of Mott-insulating state in 1T-TaS₂. *Nat. Commun.* **7**, 10956 (2016).
- Ahn, K. H., Lookman, T. & Bishop, A. R. Strain-induced metal-insulator phase coexistence in perovskite manganites. *Science* **428**, 401–404 (2004).
- Meyers, D. et al. Strain-modulated Mott transition in EuNiO₃ ultrathin films. *Phys. Rev. B* **88**, 075116 (2013).
- Svetin, D. et al. Transitions between photoinduced macroscopic quantum states in 1T-TaS₂ controlled by substrate strain. *Appl. Phys. Express* **7**, 103201 (2014).
- Torre, A. L., Botello-Mendez, A., Baaziz, W., Charlier, J. C. & Banhart, F. Strain-induced metal-semiconductor transition observed in atomic carbon chains. *Nat. Commun.* **6**, 6636 (2015).
- Gan, L. Y. et al. Strain tuning of the charge density wave in monolayer and bilayer 1T-TaS₂. *Phys. Chem. Chem. Phys.* **18**, 3080–3085 (2016).
- Zhao, R. et al. Tuning phase transitions in 1T-TaS₂ via the substrate. *Nano Lett.* **17**, 3471–3477 (2017).
- Han, Y. et al. Strain mapping of two-dimensional heterostructures with subpicometer precision. *Nano Lett.* **18**, 3746–3751 (2018).
- Dadgar, A. M. et al. Strain engineering and Raman spectroscopy of monolayer transition metal dichalcogenides. *Chem. Mater.* **30**, 5148–5155 (2018).
- Gao, S. et al. Atomic-scale strain manipulation of a charge density wave. *Proc. Natl Acad. Sci. USA* **115**, 6986–6990 (2018).
- Andrade, E. F. et al. Visualizing the nonlinear coupling between strain and electronic nematicity in the iron pnictides by elasto-scanning tunneling spectroscopy. Preprint at <https://arxiv.org/abs/1812.05287> (2018)
- Wilson, J. A., DiSalvo, F. J. & Mahajan, S. Charge-density waves and superlattices in the metallic layered transition metal dichalcogenides. *Adv. Phys.* **24**, 117–201 (1975).
- Fazekas, P. & Tosatti, E. Electrical, structural and magnetic properties of pure and doped 1T-TaS₂. *Phil. Mag. B* **39**, 229–244 (1979).
- Fazekas, P. & Tosatti, E. Charge carrier localization in pure and doped 1T-TaS₂. *Phys. B + C* **99**, 183–187 (1980).
- Cho, D., Cho, Y. H., Cheong, S. W., Kim, K. S. & Yeom, H. W. Interplay of electron-electron and electron-phonon interactions in the low-temperature phase of 1T-TaS₂. *Phys. Rev. B* **92**, 085132 (2015).
- Cho, D. et al. Correlated electronic states at domain walls of a Mott-charge-density-wave insulator 1T-TaS₂. *Nat. Commun.* **8**, 392 (2017).
- Wu, X. L. & Lieber, C. M. Direct Observation of growth and melting of the hexagonal-domain charge-density-wave phase in 1T-TaS₂ by scanning tunneling microscopy. *Phys. Rev. Lett.* **64**, 1150–1153 (1990).
- Spijkerman, A., de Boer, J. L., Meetsma, A. & Wieggers, G. A. X-ray crystal-structure refinement of the nearly commensurate phase of 1T-TaS₂ in (3+2)-dimensional superspace. *Phys. Rev. B* **56**, 13757–13767 (1997).
- Xie, S. et al. Coherent, atomically thin transition-metal dichalcogenide superlattices with engineered strain. *Science* **359**, 1131–1136 (2018).
- Okada, Y. et al. Ripple-modulated electronic structure of a 3D topological insulator. *Nat. Commun.* **3**, 1158 (2012).
- Slezak, J. A. et al. Imaging the impact on cuprate superconductivity of varying the interatomic distances within individual crystal unit cells. *Proc. Natl Acad. Sci. USA* **105**, 3203–3208 (2008).
- Zeljko, I. et al. Strain engineering Dirac surface states in heteroepitaxial topological crystalline insulator thin films. *Nat. Nanotechnol.* **10**, 849–853 (2015).
- Skolimowski, J., Gerasimenko, Y. & Žitko, R. Mottness collapse without metallisation in the domain wall of the triangular-lattice Mott insulator 1T-TaS₂. *Phys. Rev. Lett.* **122**, 036802 (2019).
- Fujii, D. et al. Electronic states of domain structure in 1T-TaS_{2-x}Se_x observed by STM/STS. *J. Phys. Conf. Ser.* **969**, 012041 (2018).
- Ritschel, T. et al. Orbital textures and charge density waves in transition metal dichalcogenides. *Nat. Phys.* **11**, 328–331 (2015).
- Hovden, R. et al. Atomic lattice disorder in charge-density-wave phases of exfoliated dichalcogenides (1T-TaS₂). *Proc. Natl Acad. Sci. USA* **113**, 11420–11424 (2016).
- Zheng, Y. et al. The study of electronic nematicity in an overdoped (Bi, Pb)₂Sr₂CuO_{6+δ} superconductor using scanning tunneling spectroscopy. *Sci. Rep.* **7**, 8059 (2017).

Acknowledgements

This work was supported by the National Basic Research Program of China (Grant No. 2015CB921004), the National Natural Science Foundation of China (Grant No. NSFC-11374260), and the Fundamental Research Funds for the Central Universities in China. J.J.G., X.L., and Y.P.S. thank the support of the National Key Research and Development Program under contracts 2016YFA0300404, the National Nature Science Foundation of China under contracts 11674326 and 11874357, the Joint Funds of the National Natural Science Foundation of China, and the Chinese Academy of Sciences' Large-Scale Scientific Facility under contracts U1832141.

Author contributions

K.L.B. and W.H.Z. conducted the STM experiment. K.L.B. analyzed the data. Z.X.W. participated in the experiment. Y.F. and Y.Z. discussed the results. J.J.G., X.L., and Y.P.S. grew the samples. K.L.B. and Y.Y. wrote the paper. Y.Y. supervised the experiment. All authors have read the paper and approved it.

Competing interests

The authors declare no competing interests.

Additional information

Supplementary information is available for this paper at <https://doi.org/10.1038/s42005-019-0247-0>.

Correspondence and requests for materials should be addressed to Y.Y.

Reprints and permission information is available at <http://www.nature.com/reprints>

Publisher's note Springer Nature remains neutral with regard to jurisdictional claims in published maps and institutional affiliations.



Open Access This article is licensed under a Creative Commons Attribution 4.0 International License, which permits use, sharing, adaptation, distribution and reproduction in any medium or format, as long as you give appropriate credit to the original author(s) and the source, provide a link to the Creative Commons license, and indicate if changes were made. The images or other third party material in this article are included in the article's Creative Commons license, unless indicated otherwise in a credit line to the material. If material is not included in the article's Creative Commons license and your intended use is not permitted by statutory regulation or exceeds the permitted use, you will need to obtain permission directly from the copyright holder. To view a copy of this license, visit <http://creativecommons.org/licenses/by/4.0/>.

© The Author(s) 2019